Chemical Science

ROYAL SOCIETY OF CHEMISTRY

EDGE ARTICLE

View Article Online
View Journal | View Issue

Cite this: *Chem. Sci.*, 2025, **16**, 4768

All publication charges for this article have been paid for by the Royal Society of Chemistry

Received 4th January 2025
Accepted 1st February 2025

DOI: 10.1039/d5sc00061k

rsc.li/chemical-science

Highly stable bismuth-chloride perovskite X-ray direct detectors with an ultralow detection limit†

Haoyu Chen,[ad] Qingyun Han,[ad] Haoming Qin,[b] Yueqi Shen,[ad] Huijun Lv,[ad] Yan Liu,[ad] Liping Du,[ad] Yong Wang,[c] Yihui He*[b] and Weihua Ning *[ad]

The quest for highly sensitive and stable X-ray detectors has intensified, driven by diverse applications such as medical diagnostics and industrial inspection. Recent strides have been made in harnessing the potential of lead halide perovskites for radiation detection, thanks to their remarkable optoelectronic properties. However, the toxicity of Pb and intrinsic material instability restrict their practical applications as next-generation efficient detectors. Here, we have developed environment-friendly three-dimensional (3D) bismuth-chloride perovskites designed for highly sensitive and stable X-ray direct detection. By the introduction of monovalent Na^+, one-dimensional (1D) $Cs_3Bi_2Cl_9$ can be converted into high-quality 3D double perovskite $Cs_2NaBiCl_6$ characterized by excellent photophysical properties. Our investigation, combining X-ray photoelectron spectroscopy and temperature-dependent photoluminescence, reveals a modulated electronic dimension and a mitigated electron–phonon coupling effect in $Cs_2NaBiCl_6$. As such, the 3D $Cs_2NaBiCl_6$-based direct detectors achieve a high sensitivity of 354.5 μC Gy^{-1} cm^{-2} and an ultralow detection limit of 59.4 nGy s^{-1}, with continuous on–off switching for 4500 s. Overall, our work provides a new direction for designing and developing lead-free perovskites to achieve highly sensitive X-ray detection with exceptional stability.

Introduction

X-ray detectors have attracted considerable attention for their wide range of applications in medical diagnostics, industrial non-destructive inspection, aerospace, high-energy physics, and scientific research.[1–4] Compared to indirect methods involving the conversion of X-ray into photons through scintillation, followed by detection *via* photodiodes, direct conversion of X-rays into an electrical signal offers superior spatial resolution and a more streamlined system configuration.[5–9] Currently, extensive research has focused on α-Se[10,11] and CdZnTe[12,13] semiconductors for their superior detection performance in the past few decades. However, these materials suffer from many limitations such as the poor X-ray absorption in α-Se[11,14] and the high synthesis cost of CdZnTe.[15] Recently, solution-processed Pb-based perovskites[16–19] with low defect density, high carrier mobility, and long carrier diffusion lengths[20] have been anticipated as the next generation of high-efficiency X-ray detectors. In particular, the reported radiation detectors based on three dimensional (3D) perovskites, such as $MAPbBr_3$,[21,22] $MAPbI_3$ (ref. 23 and 24) and $CsPbBr_3$ (ref. 25–28) have demonstrated encouraging and promising performance.

Despite their enormous success, the toxic lead content[20] and poor stability[29] are major obstacles to future commercialization. To remedy both issues, the community has now made increasing efforts on lead-free perovskites. Among these,[30–33] bismuth-based perovskites stand out for their substantial X-ray attenuation coefficient and stability. Recent reports on sensitive X-ray detectors employing either $Cs_2AgBiBr_6$ (ref. 34–36) or $(NH_4)_3Bi_2I_9$ (ref. 37) single crystals (SCs) have demonstrated sensitivity exceeding 10^3 μC Gy^{-1} cm^{-2}, outperforming commercial X-ray detectors. However, these detectors based on bismuth-bromide/iodide perovskite suffer from baseline drift and significant noise. Furthermore, the inherent chemical properties of bismuth make it challenging to form high-dimensional structures, resulting in poor charge carrier transport.[38–41] These offer significant potential to improve the performance of bismuth-based perovskites. Chlorides emerge as an ideal solution, offering high stability and a wide bandgap.[42] Our previous work confirms that replacing two Pb atoms with a combination of B(I) and Bi(III) can also lead to the formation of a 3D double perovskite structure.[34,43]

[a]*Jiangsu Key Laboratory for Carbon-Based Functional Materials & Devices, Institute of Functional Nano & Soft Materials (FUNSOM), Soochow University, Suzhou, 215123, P. R. China. E-mail: whning@suda.edu.cn*

[b]*State Key Laboratory of Radiation Medicine and Protection, Collaborative Innovation Center of Radiological Medicine of Jiangsu Higher Education Institutions, School for Radiological and Interdisciplinary Sciences (RAD-X), Soochow University, Suzhou 215123, P. R. China. E-mail: yhhe@suda.edu.cn*

[c]*State Key Laboratory of Silicon and Advanced Semiconductor Materials, School of Materials Science and Engineering, Hangzhou Global Scientific and Technological Innovation Center, Zhejiang University, Hangzhou 310027, P. R. China*

[d]*Jiangsu Key Laboratory of Advanced Negative Carbon Technologies, Soochow University, Suzhou, 215123, P. R. China*

† Electronic supplementary information (ESI) available. See DOI: https://doi.org/10.1039/d5sc00061k

Herein, we have developed environment-friendly 3D inorganic bismuth-chloride perovskite SCs designed for highly sensitive and stable X-ray detection. The introduction of monovalent metal cations Ag^+ and Na^+ convert 1D $Cs_3Bi_2Cl_9$ into a 3D double perovskite structure, optimizing the carrier transport in the low-dimensional bismuth-based perovskite. Our results demonstrate that the Na–Bi combination is advantageous compared to Ag–Bi due to the increased resistivity and weaker electron–phonon coupling, therefore leading to suppressed non-radiative recombination. The 3D $Cs_2NaBiCl_6$ SC direct detectors yield a high sensitivity of 354.5 μC Gy^{-1} cm^{-2} and an ultralow detection limit of 59.4 nGy s^{-1}, with continuous operation for up to 4500 seconds of radiation. Our work not only enriches the applications of bismuth-chloride perovskites for X-ray detection but also provides new insights for the design of efficient and stable detection materials through crystal structure design.

Results and discussion

The SCs of $Cs_3Bi_2Cl_9$, $Cs_2AgBiCl_6$ and $Cs_2NaBiCl_6$ were synthesized *via* the hydrothermal method (see details in the Experimental section). The crystal structures of $A_3B_2X_9$ perovskite have been extensively studied and characterized using zero-dimensional (0D), one-dimensional (1D), and two-dimensional (2D) clusters.[44] The $Cs_3Bi_2I_9$ crystal shows a 0D isolated cluster structure, while $Cs_3Bi_2Br_9$ exhibits a 2D layer structure (Fig. S1†). In contrast, the crystal structure of $Cs_3Bi_2Cl_9$ exhibits a perovskite-like arrangement, featuring 1D zigzag chains of *cis*-corner-shared $[BiCl_6]^{3-}$ octahedra separated by Cs^+ cations (Fig. 1). The centered bismuth atoms in $[BiCl_6]^{3-}$ octahedra are coordinated by four terminal and two neighboring bridging chloride atoms. Simultaneously, the configuration of $[BiCl_6]^{3-}$ octahedra is distorted, as evidenced by the inhomogeneity of Cl–Bi–Cl angles and Bi–Cl bond lengths (Fig. S2†). The Cs^+ cations reside in the cubo-octahedral cavities. When Na^+/Ag^+ is introduced into the 1D $Cs_3Bi_2Cl_9$ crystal structure, we observe a significant structural evolution, forming 3D double perovskite structure $Cs_2AgBiCl_6$ and $Cs_2NaBiCl_6$. For the double perovskite $Cs_2AgBiCl_6$, each Bi and Ag atom coordinates with six Cl^- ions to form $[BiCl_6]^{3-}$ and $[AgCl_6]^{5-}$ units. These units, in turn, stack alternatively as $[BiCl_6]^{3-}$ and $[AgCl_6]^{5-}$ octahedra, with Cs^+ atoms occupying the cavities in the 3D structure (Fig. 1). $Cs_2AgBiCl_6$ belongs to the cubic $Fm\bar{3}m$ space group, with cell parameters $a = b = c = 10.7505(17)$ Å. $Cs_2NaBiCl_6$ exhibits the same crystal structure with cell parameters determined to be $a = b = c = 10.8360(3)$ Å (Fig. S3†). Surprisingly, the parameter decreased upon the substitution of silver ions, despite Ag^+ having a larger effective ionic radius (115 pm) compared to Na^+ (102 pm), attributed to the covalent nature of Ag–Cl bonds in contrast to the ionic bonds of Na–Cl. The strength of Ag–Cl coordination bonds surpasses that of Na–Cl coordination bonds, as indicated by a comparison of bond lengths (Fig. S2†). A series of high-quality $Cs_3Bi_2Cl_9$, $Cs_2AgBiCl_6$ and $Cs_2NaBiCl_6$ crystals are successfully synthesized, as confirmed by Powder X-ray Diffraction (PXRD) (Fig. S4†). No impurity phase is detected in their patterns, with all diffraction peaks of the products closely matching those in the standard XRD pattern. Besides, we quantified the element content by Inductively Coupled Plasma (ICP) in Table S2.† The atomic percentage ratio of $Cs_2NaBiCl_6$ is around Cs/Na/Bi = 2 : 1 : 1, which indicates the expected composition.

To evaluate the optical properties of $Cs_3Bi_2Cl_9$, $Cs_2AgBiCl_6$ and $Cs_2NaBiCl_6$, ultraviolet-visible and photoluminescence spectroscopy are conducted (Fig. 2a). $Cs_3Bi_2Cl_9$ displays absorption before 425 nm. The introduction of monovalent metal ions induces significant changes in the absorption characteristics. $Cs_2NaBiCl_6$ reduces the absorption range to below 400 nm, while $Cs_2AgBiCl_6$ extends absorption considerably, reaching 475 nm. Similar to other double perovskites, $Cs_2AgBiCl_6$ and $Cs_2NaBiCl_6$ exhibit distinct, sharp absorption peaks, attributed to exciton absorption or to direct bismuth s–p transitions.[30,43,44] By fitting in a Tauc plot (Fig. S5†), the indirect bandgaps[45,46] for $Cs_3Bi_2Cl_9$, $Cs_2AgBiCl_6$, and $Cs_2NaBiCl_6$ are determined to be 3.0 eV, 2.6 eV, and 3.4 eV, respectively. The bandgap of $Cs_2NaBiCl_6$ is 3.4 eV with an absorption band edge at 400 nm, but appeared to be off yellow (in Fig. 1), which is attributed to the severe band-edge dragging characteristic of double perovskite, analogous to $Cs_2AgBiBr_6$.[34–36] Larger band gaps in radiation detection are expected to effectively reduce dark current and noise current.[47] In addition, the photoluminescence (PL) spectra reveal emission bands with peaks at approximately 650 nm for $Cs_2NaBiCl_6$ and 620 nm for $Cs_2AgBiCl_6$ under 365 nm excitation (Fig. 2a). Both exhibit broad PL spectra and significant Stokes shifts, characteristic of Self-Trapped Exciton (STE) formation, a common feature in other perovskites.[48,49]

To gain more insight into the photophysical mechanisms of bismuth-chloride perovskite, temperature-dependent PL is further investigated (Fig. 2b and c). At room temperature, the

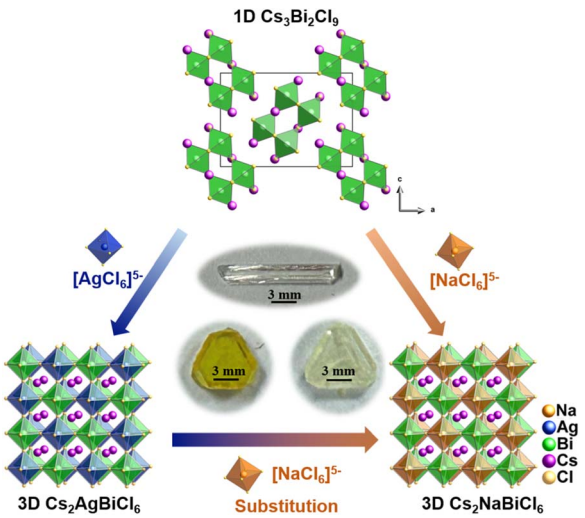

Fig. 1 The structural evolution of bismuth-chloride perovskites $Cs_3Bi_2Cl_9$, $Cs_2AgBiCl_6$ and $Cs_2NaBiCl_6$. With the introduction of monovalent cations to $Cs_3Bi_2Cl_9$, the dimension increases from 1D to 3D. Crystal photographs are included as insets to visually depict the structural changes.

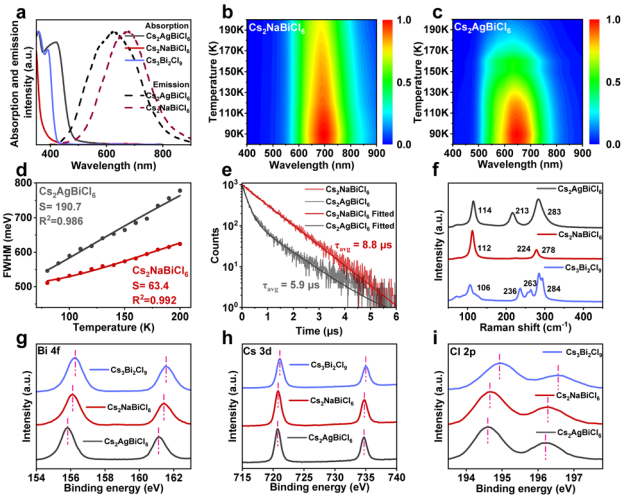

Fig. 2 (a) Absorption and PL spectra of three bismuth-chloride perovskites. (b and c) Normalized PL spectra at varying temperatures of $Cs_2NaBiCl_6$ and $Cs_2AgBiCl_6$. (d) The FWHM as a function of temperature for $Cs_2NaBiCl_6$ and $Cs_2AgBiCl_6$. (e) PL decay curves of $Cs_2NaBiCl_6$ and $Cs_2AgBiCl_6$. (f) Raman spectra. (g–i) The X-ray photoelectron spectroscopy (XPS) spectra of Bi 4f, Cs 3d and Cl 2p (observation: the experiments described above are conducted utilizing powdered specimens).

emission of $Cs_2NaBiCl_6$ is barely visible. However, upon decreasing the temperature to 80 K, an emission band emerges with a peak at around 690 nm. The PL intensity continues to increase with further temperature reduction, suggesting the suppression of nonradiative recombination at lower temperatures. A similar temperature-dependent emission trend is observed for $Cs_2AgBiCl_6$. According to the characteristic PL spectra, both double perovskites exhibit STE emissions. The formation of STEs is closely associated with electron–phonon coupling effects.[50] The electron–phonon coupling effect can intensively constrain the excitons and thereby restrain charge transport. Here, we investigate the effect of different monovalent ions (Ag *versus* Na) on the electron–phonon coupling effect. The electron–phonon coupling can be quantitatively evaluated using the Huang–Rhys factor (S), derived from the Full Width at Half Maximum (FWHM) of photoluminescence, as expressed in the following equation:[51]

$$\mathrm{FWHM} = 2.36\sqrt{S}\hbar\omega_{\mathrm{phonon}}\sqrt{\coth\frac{\hbar\omega_{\mathrm{phonon}}}{2k_{\mathrm{B}}T}} \quad (1)$$

where ω_{phonon} is the phonon frequency, T is the temperature, and k_{B} is the Boltzmann constant. As depicted in Fig. 2d, we determined the S value for pristine $Cs_2AgBiCl_6$ and $Cs_2NaBiCl_6$ by fitting the temperature-dependent FWHM of photoluminescence peaks. The S values for $Cs_2AgBiCl_6$ and $Cs_2NaBiCl_6$ are 190.7 and 63.4, respectively. In comparison to the S value of $Cs_2AgBiBr_6$ (111.3) (Fig. S8†),[52] the interaction between Na and Bi restricts the giant electron–phonon coupling, thereby mitigating the formation of STEs to some extent and benefitting the carrier transport. Besides, concerning applications in detection,[53] non-radiation recombination negatively impacts charge collection efficiency. This is further corroborated by the longer PL average lifetime of $Cs_2NaBiCl_6$ (8.8 μs) compared to $Cs_2AgBiCl_6$ (5.9 μs), indicating restrained non-radiative recombination loss, and benefiting charge separation (Fig. 2e).[54] Therefore, the weaker interaction between Na^+ and halogens, as opposed to that of $[BiX_6]^{3-}$, diminishes the giant electron–phonon coupling in the bismuth-chloride double perovskite. This insight holds significance for the design of double perovskite structures.

To further study the effect of lattice vibration on carrier transport, Raman spectroscopy is conducted at room temperature, using a 532 nm laser beam (Fig. 2f). Phases are observed in the range of 50 to 400 cm^{-1}. In the orthorhombic phase of $Cs_3Bi_2Cl_9$, there are two types of $[BiCl_6]^{3-}$ polyhedra with low symmetry (Fig. S2†). The lower symmetry of the $[BiCl_6]^{3-}$ polyhedron in the orthorhombic phase may contribute to a higher number of Raman bands, indicating more open scattering channels to enhance carrier-phonon scattering.[55] Following the assignment of analogues in previous studies of $Cs_2AgBiCl_6$,[56] the band at 115 cm^{-1} is attributed to the breathing vibration of the Ag–Cl bonds with T_{2g} symmetry. The two bands at 212 and 284 cm^{-1} correspond to the stretching vibrations of the $[AgCl_6]^{5-}$ octahedron with different vibrational symmetries of E_g and A_{1g}, respectively. Notably, due to the stronger bonding strength of Bi–Cl compared to Na–Cl, $[BiCl_6]^{3-}$ lattice vibrations in $Cs_2NaBiCl_6$ dominate the Raman spectra (Fig. S2†). The decreased intensity of the E_g vibration from $Cs_2AgBiCl_6$ to $Cs_2NaBiCl_6$ can be associated with the asymmetric stretching of the $[BiCl_6]^{3-}$ octahedron. This implies that the replacement of Na ions reduces electron–phonon interaction, weakening nonradiative transitions.

To study the difference in the electronic interaction before and after monovalent ion introduction, XPS is carried out. In the XPS spectra of Cl 2p, Bi 4f, and Cs 3d (Fig. 2g–i), the binding energy for Cl 2p shifts to a lower value after the introduction of monovalent ions, indicating an increase in electron density around Cl and a feasible electron transfer from monovalent ions to Cl. The decrease in Cl 2p electron binding energy in $Cs_2B(I)BiCl_6$ is associated with the shorter B(I)–Cl bond length compared to the Bi–Cl bond in $Cs_3Bi_2Cl_9$, resulting in a stronger interaction between B(I) and Cl (Fig. S2†). Additionally, a slight decrease in the binding energy of Bi 4f is observed for $Cs_2B(I)BiCl_6$ compared with $Cs_3Bi_2Cl_9$, ascribed to the elimination of $[BiCl_6]^{3-}$ octahedral distortion and an increase in the Cl–Bi–Cl bond angle (Fig. S2†), weakening the interaction between Bi and Cl. Compared with $Cs_3Bi_2Cl_9$, the negative shift of Cs 3d peaks in $Cs_2B(I)BiCl_6$ is indicative of increased electron density around Cs. Overall, due to structural transformations, especially the elimination of $[BiCl_6]^{3-}$ octahedral distortion, the binding energy of electrons around Cl, Bi, and Cs in $Cs_2B(I)BiCl_6$ is reduced to varying degrees, indicating more dispersed electronic distributions.[53] Moreover, the degree of negative shift is larger in $Cs_2AgBiCl_6$ than in $Cs_2NaBiCl_6$, suggesting that the conductivity of $Cs_2AgBiCl_6$ is more outstanding than that of $Cs_2NaBiCl_6$.

To evaluate the potential in X-ray detectors, we calculate the absorption coefficient of the $Cs_3Bi_2Cl_9$, $Cs_2AgBiCl_6$ and

$Cs_2NaBiCl_6$ SCs as a function of photon energy utilizing the photon cross-section database. Fig. 3a illustrates that the absorption coefficient of the three bismuth-chloride perovskite SCs is significantly higher than that of Si across the entire photon energy range, and comparable to that of the inorganic semiconductors CdTe and $Cs_2AgBiBr_6$. The X-ray attenuation formula is employed to predict the X-ray stopping ability, as follows:[57,58]

$$I = I_0 \exp(-\mu_m d) = I_0 \exp(-\alpha \rho d) \quad (2)$$

where μ_m, ρ, d and α represent the linear absorption coefficient, density, thickness of a single crystal and the X-ray absorption cross-section, respectively. By utilizing absorption coefficients for X-rays at different energies, we calculated the required thickness of various materials to achieve complete absorption of X-rays at a specific energy. Fig. 3b demonstrates that a thickness of approximately 1.0 mm is sufficient for bismuth-chloride perovskite SCs to absorb 90% of 50 keV X-rays. To evaluate the X-ray detection performance of the three SCs, detectors are fabricated with the structure shown in Fig. 3c and S10.†

To achieve high sensitivity and a low detection limit in X-ray detection materials, certain prerequisites must be met, including a high $\mu\tau$ product, large bulk resistivity, and a high on/off ratio. To determine the bulk resistivity, I–V measurements are conducted in the dark (Fig. 3d). $Cs_3Bi_2Cl_9$ has the highest resistivity, followed by $Cs_2NaBiCl_6$, and $Cs_2AgBiCl_6$. However, these values exceed that of the pristine $Cs_2AgBiBr_6$ SC (2.59×10^9 Ω cm),[34] indicating that chloride has a higher resistivity than bromide. Simultaneously, $Cs_2NaBiCl_6$ is not as conductive as $Cs_2AgBiCl_6$. $[NaX_6]^{5-}$ with high ionic bonding properties in $Cs_2NaBiCl_6$ acts as an electronic barrier, increasing the resistivity of the perovskite. Additionally, the Ag^+ with d_{10} orbitals significantly contributes to the construction of the valence band maximum (VBM), thereby improving the carrier transport. Furthermore, photoconductivity measurements were conducted, and the $\mu\tau$ product is determined by fitting the photoconductivity curve with the modified Hecht equation:[59]

$$I = \frac{I_0 \mu\tau V}{d^2}\left[1 - \exp\left(-\frac{d^2}{\mu\tau V}\right)\right] \quad (3)$$

where I_0, d, and V represent the saturated current, effective thickness, and external bias, respectively. The carrier $\mu\tau$ in the double perovskite increases by 2 to 3 times with the introduction of the monovalent cations in $Cs_3Bi_2Cl_9$, aligning with the lower binding energy observed in the XPS data (Fig. 3e). Therefore, elevating the dimensions proves to be an effective method for enhancing carrier transport. Subsequently, the on/off ratios of the three perovskites are also investigated. The $Cs_2NaBiCl_6$ compound exhibits a moderate on/off ratio of 108.8 due to its moderate resistivity and $\mu\tau$. Furthermore, $Cs_2NaBiCl_6$ displays the highest photocurrent density, attributed to its weaker electron–phonon coupling in comparison to $Cs_2AgBiCl_6$. The X-ray response of the three perovskites corresponds to their individual material characteristics.

Sensitivity is a critical parameter of the detector and requires considerable attention. To study the sensitivity of bismuth-chloride perovskites, the data of the X-ray response are evaluated. The formula for sensitivity is expressed as the difference between photocurrent and dark current per unit dose rate and unit cross-sectional area:[60]

$$S = \frac{I_p - I_d}{D \times A} \quad (4)$$

I_p represents the photogenerated current, I_d represents the dark current, D is the dose rate, and A is the effective cross-sectional area of the detector. The $Cs_2NaBiCl_6$ SCs exhibit a high sensitivity of 354.5 μC Gy^{-1} cm^{-2} when the thickness is 0.89 mm, and the working bias is 200 V, as shown in Fig. 3f. This value surpasses that of $Cs_3Bi_2Cl_9$ (281.1 μC Gy^{-1} cm^{-2}) and is approximately three times that of the $Cs_2AgBiCl_6$ SC detector (109.5 μC Gy^{-1} cm^{-2}) as shown in Fig. 3g. The X-ray detection sensitivities of bismuth-based perovskite SC detectors of different dimensions (3D, 2D and 1D) are compared as shown in Fig. 3h. $Cs_2NaBiCl_6$ and $Cs_3Bi_2Cl_9$ demonstrate relatively high sensitivity values in double perovskite and 1D bismuth-based perovskite, respectively. This highlights the potential of bismuth-chloride perovskites in X-ray direct detection.

To achieve high-performance X-ray detection, sensitivity is not the only crucial factor. The minimum detectable dose rate, also known as the detection limit, is equally important. To determine the detection limit, we calculated the signal-to-noise

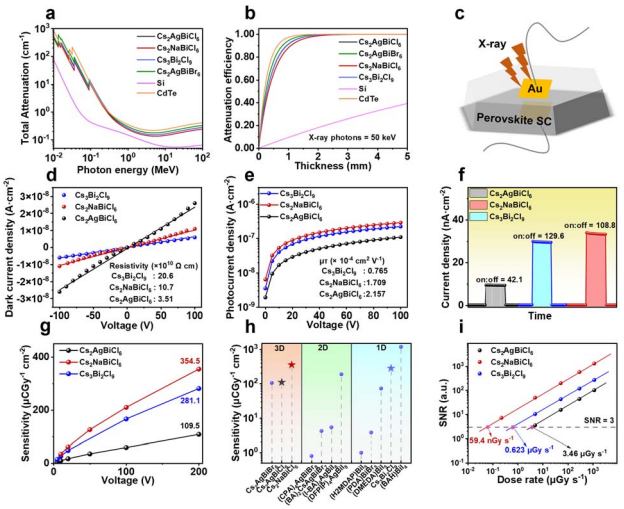

Fig. 3 (a) Absorption coefficients of semiconductors as a function of photon energy. (b) Attenuation efficiency of 50 keV X-ray photons *versus* thickness. (c) Device structure of $Cs_2AgBiCl_6$ and $Cs_2NaBiCl_6$ SC detectors. (d–f) The variations among resistance, the carrier mobility-lifetime product ($\mu\tau$) and the on/off ratio. (g) The sensitivity at different bias values. (h) Comparison of sensitivity among 3D, 2D and 1D bismuth-based perovskite X-ray detectors. (i) X-ray dose rate-dependent signal-to-noise ratio (SNR) at 10 V bias. (Six single crystal devices are prepared for each single crystal shown in Tables S3–S5.† The resistivity of a single crystal can be used to assess its quality. Higher resistivity is indicative of superior crystal quality, and thus, we selected the single crystal with the highest resistivity for subsequent experiments.)

ratio (SNR) of the response current at different dose rates. The SNR as a function of dose rate is shown in Fig. 3i. According to the International Union of Pure and Applied Chemistry (IUPAC) definition, the detection limit is equal to the dose rate that can generate an average response signal larger than 3 times the signal noise. To obtain the X-ray response at lower dose rates, we use aluminum foil to block the radiation and accurately calibrated the corresponding dose rates as shown in Fig. S18.† In this work, we extended the fitting line of the dose-rate-dependent SNR to 3, determining the detection limit of the $Cs_2NaBiCl_6$ SC detector to be 59.4 nGy s^{-1} at a 10 V bias. This result showcases the lowest detection limit in 3D double bismuth-based perovskite.

The X-ray response of $Cs_2NaBiCl_6$ SC detectors is excellent due to their exceptional crystal quality and optoelectronic properties. Their dose-rate dependent net photocurrent densities at different bias voltages are shown in Fig. S12,† illustrating the signal current density of $Cs_3Bi_2Cl_9$, $Cs_2AgBiCl_6$ and $Cs_2NaBiCl_6$ devices at different biases and dose rates.

To study the stability of the bismuth-chloride perovskites, thermogravimetric analysis (TGA) and XRD are performed. Fig. 4a shows the TGA results for the decomposition of $Cs_3Bi_2Cl_9$, $Cs_2AgBiCl_6$, and $Cs_2NaBiCl_6$ SCs. Notably, $Cs_2NaBiCl_6$ exhibits a high decomposition initiation temperature of 505 °C. In comparison, $Cs_2AgBiBr_6$ and $Cs_3Bi_2Br_9$ SCs begin to decompose at 430 °C and 350 °C, respectively.[61] Furthermore, after 1 year under atmospheric conditions and at a temperature of 25 °C, $Cs_2NaBiCl_6$ demonstrates exceptional environmental stability, as evidenced by the consistent FWHM of the peak (220) compared to that one year ago shown in Fig. 4b. In addition, to trace the changes in the oxidation state, environment and halogen migration, fitted XPS parameters of the central metal ion and halogen have been provided before and after X-ray detection in Fig. S19.† It is established that the binding energies of the elements of bismuth chloride-based perovskite are not significantly changed before and after X-ray irradiation, suggesting that consistent chemical and physical properties were maintained after irradiation. Besides, we evaluated the trap-state density of the $Cs_2NaBiCl_6$ SCs using a space-charge-limited current (SCLC) method. It shows a n_{trap} of 1.20 × 10^{10} cm^{-3}, which is only a 13% improvement over that of the newly made device. And μ is found to be 1.24 × 10^{-4} cm^2 V^{-1} s^{-1}, which is reduced by 23% compared to that of freshly made devices in Fig. S20.† This demonstrates that $Cs_2NaBiCl_6$ SC devices have good stability.

To study the device stability, the long-term operation and a series of on–off switches are investigated. The dark current drift (I_{drift}) is another vital parameter of X-ray detectors, obtained by using:[62]

$$I_{drift} = \frac{I_t - I_0}{E \times A \times t} \quad (5)$$

where I_0 and I_t are the current initially and at time t, respectively, E is the electric field, and A is the device area. As shown in Fig. 4c and S21,† we observe a highly stable dark current drift of 1.30 × 10^{-8} nA cm^{-1} s^{-1} V^{-1} at 10 V bias and 7.9 × 10^{-7} nA cm^{-1} at 100 V bias. Among the three-dimensional (3D) structures, the lead-free double perovskite exhibits a lower baseline drift, while $Cs_2NaBiCl_6$ has a more stable baseline compared to conventional $Cs_2AgBiBr_6$ shown in Table S6.† Importantly, its exceptional radiation stability is highlighted by the fact that there is no significant change in photocurrent under X-ray exposure. Additionally, Fig. 4d illustrates barely noticeable decay in the X-ray response after a continuous series of on–off switches over 4500 s (atmosphere, R. T.). As demonstrated, these outstanding stabilities provide the $Cs_2NaBiCl_6$ X-ray detectors with significant potential for operation in harsh environments.

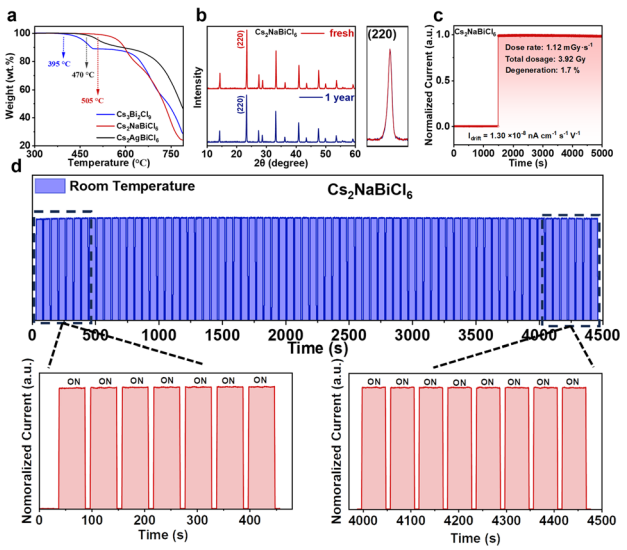

Fig. 4 (a) TGA comparison of $Cs_3Bi_2Cl_9$, $Cs_2AgBiCl_6$ and $Cs_2NaBiCl_6$. (b) XRD patterns before and after ambient storage (1 year) of $Cs_2NaBiCl_6$. (c) Dark current tracking of the detector and photo response of the $Cs_2NaBiCl_6$ SC device under continuous X-ray irradiation. (d) On–off stability to X-rays at room temperature.

Conclusions

In conclusion, we have demonstrated novel bismuth-chloride perovskites for highly sensitive and stable X-ray detection. By the introduction of monovalent metal cations, silver, and sodium, 1D $Cs_3Bi_2Cl_9$ can be converted to 3D double perovskite with alternating $[B(I)Cl_6]^{5-}$ (B = Ag, Na) and $[BiCl_6]^{3-}$ octahedra, optimizing the optoelectronic properties and increasing the electronic dimensions. The compositional substitution strategy (Ag *versus* Na) allows for versatile tuning of high resistivity and high $\mu\tau$, which are typically contradictory parameters for radiation detection. Besides, temperature-dependent PL as well as Raman spectroscopy robustly confirm that 3D $Cs_2NaBiCl_6$ can significantly reduce the giant electron–phonon coupling effect, which is widely present in double perovskites. The optimized 3D $Cs_2NaBiCl_6$ devices exhibit a high sensitivity of 354.5 μC Gy^{-1} cm^{-2} and a low detection limit of 59.4 nGy s^{-1} at an external bias of 10 V, demonstrating long-term operational stability. Our results also suggest a new direction for the design of a lead-free perovskite to realize highly sensitive X-ray

detection with extreme stability, potentially stimulating further exploration of lead-free perovskites for diverse applications.

Data availability

The data that support the findings of this study are available in the ESI† of this article.

Author contributions

H. Chen and W. Ning conceived the idea for the manuscript and designed the experiments; H. Chen and Q. Han developed the synthesis procedures and performed the basic chemical and physical characterization; Y. Shen participated in the SC-XRD characterization; H. Qin assisted in the data analysis; W. Ning and Y. He guided the experiments, discussed the data, and led the project; H. Chen wrote the original draft and W. Ning, Y. He, Y. Wang, Y. Liu, and H. Lv reviewed and edited the draft.

Conflicts of interest

There are no conflicts to declare.

Acknowledgements

The authors thank Feng Gao (Linköping University, Sweden) for insightful discussions. This work was supported by the Suzhou Key Laboratory of Functional Nano & Soft Materials, the Collaborative Innovation Center of Suzhou Nano Science & Technology, the 111 Project, the Joint International Research Laboratory of Carbon-Based Functional Materials and Devices, the National Natural Science Foundation of China (22103054 and 22161132026), the Gusu Innovation and Entrepreneurship Leading Talent Program (ZXL2023188), and the Jiangsu Key Laboratory for Carbon-Based Functional Materials and Devices (Z221311). Y. H. thanks the National Key R&D Program of China (2021YFF0502600 and 2021YFB3201000), the National Natural Science Foundation of China (U2267211), the Jiangsu Natural Science Foundation (BK20210711) and the Suzhou Innovation and Entrepreneurship Leading Talent Plan Project. Y. W. thanks the National Natural Science Foundation of China (No. 52302315) and the talent project of the ZJU-Hangzhou Global Scientific and Technological Innovation Center (No. 02170000-K02013017).

Notes and references

1 C. Szeles, *Phys. Status Solidi B*, 2004, **241**, 783–790.
2 H. Wei and J. Huang, *Nat. Commun.*, 2019, **10**, 1066.
3 W. H. a. C. Brabec, *Nat. Photonics*, 2016, **10**, 288–289.
4 L. B. Martin Hoheisel, *J. Non-Cryst. Solids*, 2001, **266**, 1152–1157.
5 V. V. Nagarkar, S. R. Miller, S. V. Tipnis, A. Lempicki, C. Brecher and H. Lingertat, *Nucl. Instrum. Methods Phys. Res., Sect. B*, 2004, **213**, 250–254.
6 D. Pacella, *Rep. Med. Imaging*, 2015, **8**, 1–13.
7 F. Cao, D. Yu, W. Ma, X. Xu, B. Cai, Y. M. Yang, S. Liu, L. He, Y. Ke, S. Lan, K.-L. Choy and H. Zeng, *ACS Nano*, 2020, **14**, 5183–5193.
8 Y. Huang, L. Qiao, Y. Jiang, T. He, R. Long, F. Yang, L. Wang, X. Lei, M. Yuan and J. Chen, *Angew. Chem., Int. Ed.*, 2019, **58**, 17834–17842.
9 F. Yao, K. Dong, W. Ke and G. Fang, *ACS Nano*, 2024, **18**, 6095–6110.
10 H. Huang and S. Abbaszadeh, *IEEE Sens. J.*, 2020, **20**, 1694–1704.
11 S. O. Kasap, *J. Phys. D: Appl. Phys.*, 2000, **33**, 2853–2865.
12 Z. Chen, Y. Zhu and Z. He, *Nucl. Instrum. Methods Phys. Res., Sect. A*, 2020, **980**, 164501.
13 S. Del Sordo, L. Abbene, E. Caroli, A. M. Mancini, A. Zappettini and P. Ubertini, *Sensors*, 2009, **9**, 3491–3526.
14 S. Kasap, J. B. Frey, G. Belev, O. Tousignant, H. Mani, J. Greenspan, L. Laperriere, O. Bubon, A. Reznik, G. DeCrescenzo, K. S. Karim and J. A. Rowlands, *Sensors*, 2011, **11**, 5112–5157.
15 S. K. Chaudhuri, K. Nguyen, R. O. Pak, L. Matei, V. Buliga, M. Groza, A. Burger and K. C. Mandal, *IEEE Trans. Nucl. Sci.*, 2014, **61**, 793–798.
16 J. Zhang, G. Hodes, Z. Jin and S. F. Liu, *Angew. Chem., Int. Ed.*, 2019, **58**, 15596–15618.
17 C. H. Kang, I. Dursun, G. Liu, L. Sinatra, X. Sun, M. Kong, J. Pan, P. Maity, E.-N. Ooi, T. K. Ng, O. F. Mohammed, O. M. Bakr and B. S. Ooi, *Light: Sci. Appl.*, 2019, **8**, 94.
18 M. Liu, M. B. Johnston and H. J. Snaith, *Nature*, 2013, **501**, 395–398.
19 H. Yi, *Science*, 2017, **358**, 1192–1197.
20 H. Wei, *Science*, 2021, **371**, 1359–1364.
21 H. Wei, Y. Fang, P. Mulligan, W. Chuirazzi, H.-H. Fang, C. Wang, B. R. Ecker, Y. Gao, M. A. Loi, L. Cao and J. Huang, *Nat. Photonics*, 2016, **10**, 333–339.
22 W. Wei, Z. Yang, X. Qiang, W. Haotong, F. Yanjun, W. Qi, D. Yehao, L. Tao, G. Alexei, C. Lei and H. Jinsong, *Nat. Photonics*, 2017, **11**, 315–321.
23 Y. Song, L. Li, M. Hao, W. Bi, A. Wang, Y. Kang, H. Li, X. Li, Y. Fang, D. Yang and Q. Dong, *Adv. Mater.*, 2021, **33**, 2103078.
24 W. Wang, H. Meng, H. Qi, H. Xu, W. Du, Y. Yang, Y. Yi, S. Jing, S. Xu, F. Hong, J. Qin, J. Huang, Z. Xu, Y. Zhu, R. Xu, J. Lai, F. Xu, L. Wang and J. Zhu, *Adv. Mater.*, 2020, **32**, 2001540.
25 Y. He, W. Ke, G. C. B. Alexander, K. M. McCall, D. G. Chica, Z. Liu, I. Hadar, C. C. Stoumpos, B. W. Wessels and M. G. Kanatzidis, *ACS Photonics*, 2018, **5**, 4132–4138.
26 Y. He, Z. Liu, K. M. McCall, W. Lin, D. Y. Chung, B. W. Wessels and M. G. Kanatzidis, *Nucl. Instrum. Methods Phys. Res., Sect. A*, 2019, **922**, 217–221.
27 Y. He, L. Matei, H. J. Jung, K. M. McCall, M. Chen, C. C. Stoumpos, Z. Liu, J. A. Peters, D. Y. Chung, B. W. Wessels, M. R. Wasielewski, V. P. Dravid, A. Burger and M. G. Kanatzidis, *Nat. Commun.*, 2018, **9**, 1609.
28 Y. He, M. Petryk, Z. Liu, D. G. Chica, I. Hadar, C. Leak, W. Ke, I. Spanopoulos, W. Lin, D. Y. Chung, B. W. Wessels, Z. He and M. G. Kanatzidis, *Nat. Photonics*, 2020, **15**, 36–42.

29 W. Ke and M. G. Kanatzidis, *Nat. Commun.*, 2019, **10**, 965.
30 W. Ning and F. Gao, *Adv. Mater.*, 2019, **31**, e1900326.
31 W. Ning, F. Wang, B. Wu, J. Lu, Z. Yan, X. Liu, Y. Tao, J.-M. Liu, W. Huang, M. Fahlman, L. Hultman, T. C. Sum and F. Gao, *Adv. Mater.*, 2018, **30**, 1706246.
32 J. Yang, C. Bao, W. Ning, B. Wu, F. Ji, Z. Yan, Y. Tao, J. M. Liu, T. C. Sum, S. Bai, J. Wang, W. Huang, W. Zhang and F. Gao, *Adv. Opt. Mater.*, 2019, **7**, 1801732.
33 K. Dong, H. Zhou, W. Shao, Z. Gao, F. Yao, M. Xiao, J. Li, Y. Liu, S. Wang, S. Zhou, H. Cui, M. Qin, X. Lu, C. Tao, W. Ke and G. Fang, *ACS Nano*, 2023, **17**, 1495–1504.
34 W. Pan, H. Wu, J. Luo, Z. Deng, C. Ge, C. Chen, X. Jiang, W.-J. Yin, G. Niu, L. Zhu, L. Yin, Y. Zhou, Q. Xie, X. Ke, M. Sui and J. Tang, *Nat. Photonics*, 2017, **11**, 726–732.
35 W. Yuan, G. Niu, Y. Xian, H. Wu, H. Wang, H. Yin, P. Liu, W. Li and J. Fan, *Adv. Funct. Mater.*, 2019, **29**, 1900234.
36 X. Zhang, T. Zhu, C. Ji, Y. Yao and J. Luo, *J. Am. Chem. Soc.*, 2021, **143**, 20802–20810.
37 R. Zhuang, X. Wang, W. Ma, Y. Wu, X. Chen, L. Tang, H. Zhu, J. Liu, L. Wu, W. Zhou, X. Liu and Y. Yang, *Nat. Photonics*, 2019, **13**, 602–608.
38 Y. Zhang, Y. Liu, Z. Xu, H. Ye, Z. Yang, J. You, M. Liu, Y. He, M. G. Kanatzidis and S. F. Liu, *Nat. Commun.*, 2020, **11**, 2304–2315.
39 C. Ma, H. Li, M. Chen, Y. Liu, K. Zhao and S. Liu, *Adv. Funct. Mater.*, 2022, **32**, 2202160.
40 Y. He, I. Hadar and M. G. Kanatzidis, *Nat. Photonics*, 2021, **16**, 14–26.
41 M. Xia, J. H. Yuan, G. Niu, X. Du, L. Yin, W. Pan, J. Luo, Z. Li, H. Zhao, K. H. Xue, X. Miao and J. Tang, *Adv. Funct. Mater.*, 2020, **30**, 1910648.
42 Y. He, C. C. Stoumpos, I. Hadar, Z. Luo, K. M. McCall, Z. Liu, D. Y. Chung, B. W. Wessels and M. G. Kanatzidis, *J. Am. Chem. Soc.*, 2021, **143**, 2068–2077.
43 A. H. Slavney, T. Hu, A. M. Lindenberg and H. I. Karunadasa, *J. Am. Chem. Soc.*, 2016, **138**, 2138–2141.
44 S. Attique, N. Ali, S. Ali, R. Khatoon, N. Li, A. Khesro, S. Rauf, S. Yang and H. Wu, *Adv. Sci.*, 2020, **7**, 1903143.
45 S. Dan, A. Maiti, S. Chatterjee and A. J. Pal, *J. Phys.: Condens. Matter*, 2021, **33**, 485701.
46 T. Luo and J. Wei, *Mater. Chem. Phys.*, 2020, **253**, 123374.
47 S. Yirong, M. Wenbo and Y. Yang, *J. Semicond.*, 2020, **41**, 051204.
48 K. M. McCall, C. C. Stoumpos, S. S. Kostina, M. G. Kanatzidis and B. W. Wessels, *Chem. Mater.*, 2017, **29**, 4129–4145.
49 F. Jiang, Z. Wu, M. Lu, Y. Gao, X. Li, X. Bai, Y. Ji and Y. Zhang, *Adv. Mater.*, 2023, **35**, 2211088.
50 C. Zhu, J. Jin, Z. Wang, Z. Xu, M. C. Folgueras, Y. Jiang, C. B. Uzundal, H. K. D. Le, F. Wang, X. Zheng and P. Yang, *Science*, 2024, **383**, 86–93.
51 S. Li, J. Luo, J. Liu and J. Tang, *J. Phys. Chem. Lett.*, 2019, **10**, 1999–2007.
52 J. A. Steele, P. Puech, M. Keshavarz, R. Yang, S. Banerjee, E. Debroye, C. W. Kim, H. Yuan, N. H. Heo, J. Vanacken, A. Walsh, J. Hofkens and M. B. J. Roeffaers, *ACS Nano*, 2018, **12**, 8081–8090.
53 L. Wan, R. Zhang, E. Cho, H. Li, V. Coropceanu, J.-L. Brédas and F. Gao, *Nat. Photonics*, 2023, **17**, 649–655.
54 M. Shi, G. Li, W. Tian, S. Jin, X. Tao, Y. Jiang, E. A. Pidko, R. Li and C. Li, *Adv. Mater.*, 2020, **32**, 2002137.
55 J. Jiang, G. Niu, L. Sui, X. Wang, Y. Zhang, L. Che, G. Wu, K. Yuan and X. Yang, *J. Phys. Chem. Lett.*, 2021, **12**, 7285–7292.
56 Y. Pei, D. Tu, C. Li, S. Han, Z. Xie, F. Wen, L. Wang and X. Chen, *Angew. Chem., Int. Ed.*, 2022, **61**, e202205276.
57 J. Liu, B. Shabbir, C. Wang, T. Wan, Q. Ou, P. Yu, A. Tadich, X. Jiao, D. Chu, D. Qi, D. Li, R. Kan, Y. Huang, Y. Dong, J. Jasieniak, Y. Zhang and Q. Bao, *Adv. Mater.*, 2019, **31**, 1901644.
58 F. Maddalena, L. Tjahjana, A. Xie, Arramel, S. Zeng, H. Wang, P. Coquet, W. Drozdowski, C. Dujardin, C. Dang and M. Birowosuto, *Crystals*, 2019, **9**, 88.
59 C. C. Stoumpos, C. D. Malliakas, J. A. Peters, Z. Liu, M. Sebastian, J. Im, T. C. Chasapis, A. C. Wibowo, D. Y. Chung, A. J. Freeman, B. W. Wessels and M. G. Kanatzidis, *Cryst. Growth Des.*, 2013, **13**, 2722–2727.
60 Y. Liu, Y. Zhang, X. Zhu, J. Feng, I. Spanopoulos, W. Ke, Y. He, X. Ren, Z. Yang, F. Xiao, K. Zhao, M. Kanatzidis and S. F. Liu, *Adv. Mater.*, 2021, **33**, e2006010.
61 X. Li, P. Zhang, Y. Hua, F. Cui, X. Sun, L. Liu, Y. Bi, Z. Yue, G. Zhang and X. Tao, *ACS Appl. Mater. Interfaces*, 2022, **14**, 9340–9351.
62 S. You, Z. K. Zhu, S. Dai, J. Wu, Q. Guan, T. Zhu, P. Yu, C. Chen, Q. Chen and J. Luo, *Adv. Funct. Mater.*, 2023, **33**, 2303523.